X-ray imaging of water motion during capillary imbibition: A study on how compaction bands impact fluid flow in Bentheim sandstone

A. Pons,[1] C. David,[2] J. Fortin,[1] S. Stanchits,[3] B. Menéndez,[2] and J. M. Mengus[4]

Received 3 September 2010; revised 20 December 2010; accepted 5 January 2011; published XX Month 2011.

[1] To investigate the effect of compaction bands (CB) on fluid flow, capillary imbibition experiments were performed on Bentheim sandstone specimens (initial porosity ~22.7%) using an industrial X-ray scanner. We used a three-step procedure combining (1) X-ray imaging of capillary rise in intact Bentheim sandstone, (2) formation of compaction band under triaxial tests, at 185 MPa effective pressure, with acoustic emissions (AE) recording for localization of the induced damage, and (3) again X-ray imaging of capillary rise in the damaged specimens after the unloading. The experiments were performed on intact cylindrical specimens, 5 cm in diameter and 10.5 cm in length, cored in different orientations (parallel or perpendicular to the bedding). Analysis of the images obtained at different stages of the capillary imbibition shows that the presence of CB slows down the imbibition and disturbs the geometry of water flow. In addition, we show that the CB geometry derived from X-ray density maps analysis is well correlated with the AE location obtained during triaxial test. The analysis of the water front kinetics was conducted using a simple theoretical model, which allowed us to confirm that compaction bands act as a barrier for fluid flow, not fully impermeable though. We estimate a contrast of permeability of a factor of ~3 between the host rock and the compaction bands. This estimation of the permeability inside the compaction band is consistent with estimations done in similar sandstones from field studies but differs by 1 order of magnitude from estimations from previous laboratory measurements.

Citation: Pons, A., C. David, J. Fortin, S. Stanchits, B. Menéndez, and J. M. Mengus (2011), X-ray imaging of water motion during capillary imbibition: A study on how compaction bands impact fluid flow in Bentheim sandstone, *J. Geophys. Res.*, *116*, XXXXXX, doi:10.1029/2010JB007973.

1. Introduction

[2] In porous sedimentary rocks, strain localization commonly develops along shear bands or compaction bands (CB). Whereas shear localization is associated with dilatant or compactive volumetric strain [*Wong et al.*, 1997], compaction bands are always associated with a reduction in porosity. As a consequence, these two localized modes of failure can significantly impact the regional fluid flow [*Antonellini and Aydin*, 1994; *Sternlof et al.*, 2006].

[3] Compaction bands are thin zones with significant reduced porosity that form normal to the most compressive stress. Such structures are observed in a wide range of high-porosity sandstones in field [*Mollema*, 1996; *Aydin and Ahmadov*, 2009; *Schultz*, 2009] as well in laboratory experiments [*Olsson and Holcomb*, 2000; *Klein et al.*, 2001; *Baud et al.*, 2004; *Fortin et al.*, 2009; *Stanchits et al.*, 2009]. Millimeters thick and centimeters in planar extend in the laboratory, or centimeters thick and tens of meters in planar extend in the field, compaction bands always present a drastic reduction in porosity: only a few percent in the compaction band compared to the range of 18–25% porosity in the intact sandstone. As a consequence, such changes in the pore structure (variations in both pore throat diameter and connectivity are expected) directly affect fluids paths and more generally the permeability of the sedimentary rock. Indeed, it has been shown that compaction bands act as a barrier for the fluid flow. More precisely, *Aydin and Ahmadov* [2009] report in the field a contrast of permeability of a factor of ~5 between the host rock and the compaction bands, whereas a contrast in a larger range of 20–400 is reported in the laboratory [*Vajdova et al.*, 2004].

[4] In the laboratory, the estimation of the effect of one compaction band on the rock permeability is not obvious: indeed, during deformation several compaction bands can occur; thus, the measured permeability depends one this complex structure. Then the permeability inside one com-

[1]École normale supérieure de Paris, Laboratoire de Géologie, UMR CNRS 8538, Paris, France.
[2]Laboratoire Géosciences et Environnement Cergy, Université de Cergy-Pontoise, Cergy-Pontoise, France.
[3]German Research Center for Geosciences, GFZ Potsdam, Potsdam, Germany.
[4]IFP Énergies Nouvelles, Rueil-Malmaison, France.

0148-0227/11/2010JB007973

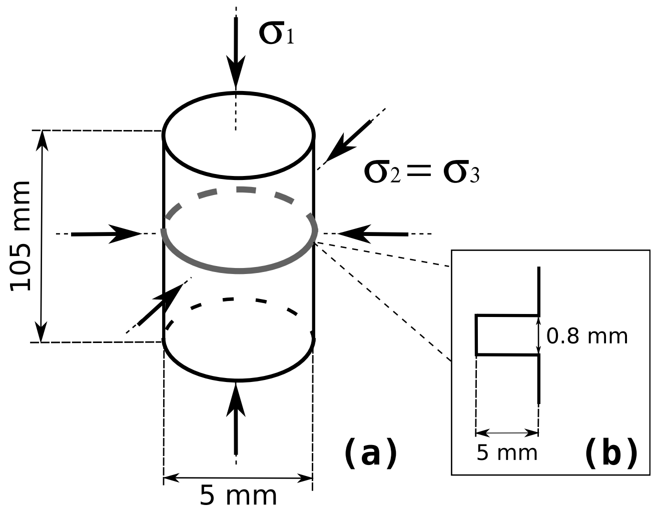

Figure 1. (a) Geometric configuration of a specimen in a triaxal test and (b) notch geometry.

paction band, K_{CB}, should be deduced by taking into account the number of localizations measured after loading considering that the permeability of the specimen equals the permeability of a series of compacted layers (permeability K_{CB}) embedded in the intact rock (permeability K_{intact}) [*Vajdova et al.*, 2004; *Fortin et al.*, 2005]. In addition, in their estimation, *Vajdova et al.* [2004] make the assumption that all the compaction bands are crosscutting the entire specimen, which may be not always the case, as has been shown by the localization of the AE [*Fortin et al.*, 2006; *Stanchits et al.*, 2009].

[5] X-ray imaging can be a useful imaging technique for characterizing fluid flow patterns [*David et al.*, 2008]. We follow a three steps methodology combining (1) X-ray imaging of capillary rise in intact Bentheim sandstone, (2) formation of compaction band under triaxial tests with AE recording for localization of the induced damage, and (3) again X-ray imaging of capillary rise in the damaged specimens after unloading. Doing so, we intend to address the following questions. How compaction bands modify flow in a sandstone? What can we learn from capillary rise experiments on microstructural changes in a compaction band? Can we estimate the change in rock permeability due to compaction bands from capillary imbibition kinetics?

2. Experimental Details

2.1. Rock Specimens

[6] A set of three cylindrical notched specimens were prepared at the GeoForschungsZentrum (GFZ Potsdam, Germany) from a block of Bentheim sandstone (Romberg quarry, Northwestern Germany). Bentheim sandstone is a Lower Cretaceous, homogeneous, yellow sandstone with a porosity, determined by mercury porosimetry, of ~22.7% for this block which is slightly higher than the one used in previous studies [*David et al.*, 2008, 2011]. Results of mercury porosimetry present a range of pore entry radii between 5 and 25 μm with a peak clearly defined at 13.5 μm. The three specimens have a 50 mm diameter and 105 mm length. A 0.8 mm wide and 5 mm deep circumferential notch has been machined in the central part of the specimen (Figure 1). The purpose of this notch is to guide the development of compaction band [*Tembe et al.*, 2006; *Stanchits et al.*, 2009]. Neither polishing nor ultrasonic cleaning was applied. After cleaning the specimens by flushing water, they were dried in an oven at 60°C for at least 24 h. Then, to avoid any variability between the imbibition experiments before and after mechanical deformation, patches of epoxy were put, at the location of the piezoelectric transducers, before the first imbibition experiment. Two specimens were cored parallel to bedding (specimens Z1 and Z2), and one perpendicular to bedding (specimen X2). Petrophysical properties and some relevant attributes for each specimen are provided in Table 1.

2.2. Experimental Procedure

[7] A three-step procedure was followed [*David et al.*, 2008]: step 1, the dry intact specimens are placed inside an X-ray CT scanner during the capillary imbibition in order to monitor the water motion inside the rock; step 2, the specimens are then deformed under a triaxial loading, with an AE recording, in order to induce compaction bands (CB); and step 3, a second identical capillary imbibition run is finally performed on the deformed specimens.

2.3. Generation of Compaction Bands, Mechanical Data, and Acoustic Emissions

2.3.1. Mechanical Data

[8] In this paper we use the convention that compressive stresses and compactive strains are positive. The terms σ_1 and σ_3 represent the maximum and the minimum principal stresses. The experiments were performed at the GeoForschungsZentrum (Potsdam, Germany) under a constant axial displacement rate of 20 μm/min (strain rate $\dot{\varepsilon}$ = 2 × 10^{-4} s^{-1}), using a servohydraulic loading frame from Material Testing Systems (MTS) with a load capacity of 4600 kN and a maximum confining pressure of 200 MPa. The axial load was measured with an external load cell with an accuracy of 1 kN and corrected for seal friction of the loading piston.

[9] The specimens were saturated with distilled water and deformed under drained condition at a constant pore pressure, P_p = 10 MPa. The recording of the pore volume variation during loading allowed the monitoring of the evolution of connected pore volume from which volumetric strain can be deduced. The effective confining pressure, P_c, was maintained constant for all experiments, at $P_{eff} = P_c - P_p$ =

Table 1. Properties of Each Specimen

	X2	Z1	Z2
Coring direction with respect to the bedding	perpendicular	parallel	parallel
Porosity (%)		22.7 ± 0.2	
Mean grain diameter (μm)		210[a]	
Composition		Quartz(95%) Clay(5%)[b]	
Peak on Hg porosimetry spectrum (diameter in μm)		26.2	
Permeability (mdarcy)	900	1100	1100

[a]*Klein and Reuschlé* [2003].
[b]*Van Bareen et al.* [1990].

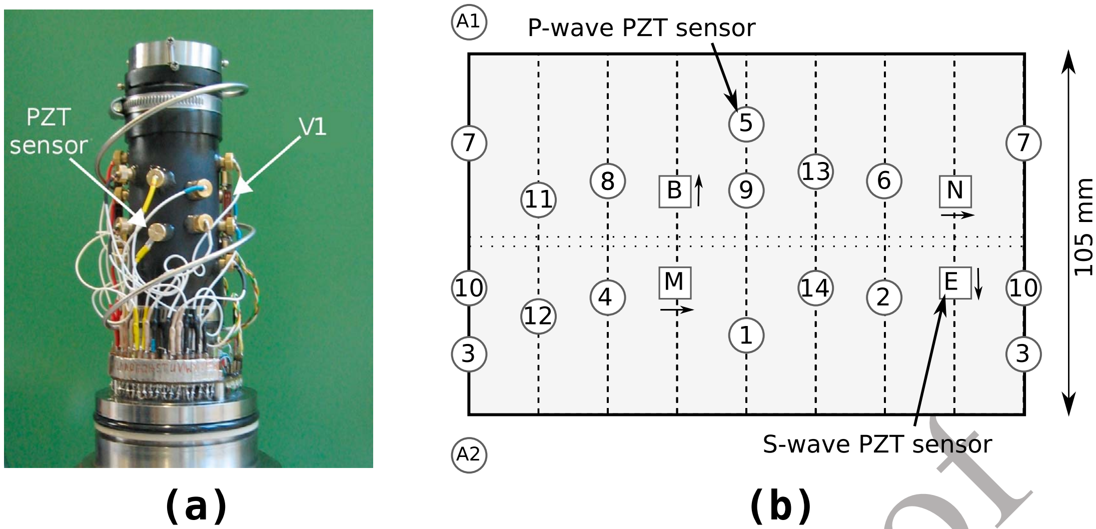

Figure 2. (a) Picture of the specimen set up and (b) map of the outside surface of the specimen showing location of the different PZT.

185 MPa. The notch was filled with a Teflon O ring ~0.7 mm thick to prevent rupture of the Neoprene jacket used to separate specimens from the oil confining medium. The axial strain, ε_{ax}, was measured by a linear variable displacement transducer (LVDT) mounted at the end of the piston and corrected for the effective stiffness of the loading frame. In addition, two vertical extensometers (V1 and V2), mounted directly on the specimen, measured shortening between the upper and the lower halves of the specimen (Figure 2a). The monitoring of these mechanical data (stress and strain) during experiments allowed us to follow the formation of CB.

2.3.2. Acoustic Emissions

[10] To monitor the AE activity during loading, 12 piezoelectric P wave and four piezoelectric S wave sensors (PZT, 1 MHz resonant frequency) were glued directly onto the surface of the rock and sealed in the jacket with a two-component epoxy (Figure 2). Two additional P wave sensors were installed in the axial direction (A1 and A2 in Figure 2b). The AE signals recording and hypocenter localization methodology are described by *Stanchits et al.* [2009]. Hypocenter location is determined with an accuracy <2 mm.

2.4. Capillary Imbibition Experiments and X-Ray Imaging

[11] The capillary imbibition procedure can be described as follows: a dry specimen is placed on a stand inside the X-ray CT scanner, such that its bottom surface is at the same level as the free surface of water reservoir which is maintained constant during the all experiment by a continuous water supply. The scanner used is a GE Hispeed Fxi CT Scanner. The X-ray tube voltage goes up to 140 kV, and current to 350 mA. The detector is composed of 816 channels high-resolution Hilight solid-state detector. During imbibition, the scanner records one image of the central cross section of the specimen every 3 s. This image corresponds to a density map averaged over a 1 mm thickness slice. The lateral resolution of the scanner used is about 400 μm. As the resolution is about twice the grain size, the intensity of each pixel of the X-ray images corresponds to the average density of a volume including several grains and pores.

[12] The analysis of the X-ray images was performed with ImageJ [*Abramoff et al.*, 2004] and can be explained as follows: first, a contrast enhancement technique was applied to the raw images (Figure 3a) in order to improve the interpretation of the images (Figure 3b). Then, we improved the image analysis method used by *David et al.* [2008] in order to extract a better geometry of the water front at each time step (Figure 3b). In contrast with the former technique where the water front geometry is approximated by an arc of circle, we use here a parabolic fit (Figure 3c). The extraction method of the water front usually provides 200 points or more which permits a robust fit of the front by the following formula at every time step: $y(x) = c_1 - c_2x^2$, where x is the horizontal distance from the center and c_1 and c_2 are two constants.

[13] From these curves (Figure 3d), the heights of water front both in the center and at the vertical borders of the specimen are estimated as a function of time. We also estimate the local radius of curvature in the center of the specimen from the fitting equation.

3. Results

[14] In the following, we first present data from capillary imbibition experiment done on intact specimens, then the mechanical data obtained in step 2, and finally, the capillary imbibition data from experiments done on deformed specimens with emphasis on the comparison with the results obtained in intact specimens.

3.1. Capillary Imbibition Experiments on Intact Specimens

3.1.1. Geometry of the Water Front

[15] The water front during imbibition is not flat but curved (Figure 3). This geometry can be quantified by the

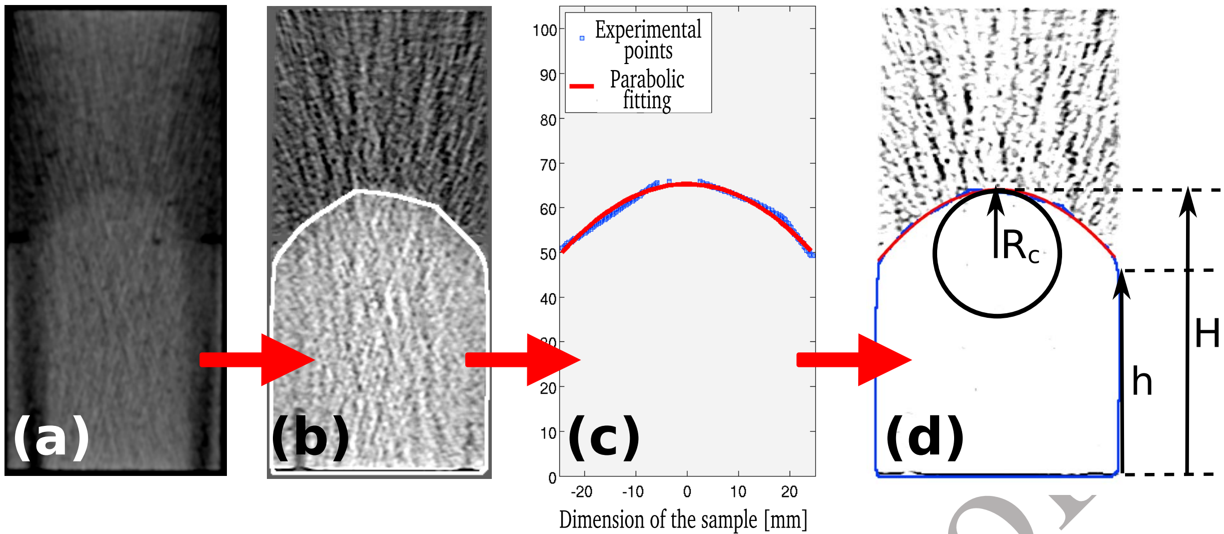

Figure 3. Summary of the image analysis procedure. (a) Raw image, (b) extraction of the edge of wet zone, (c) parabolic fit of the water front, and (d) measure of different parameters.

radius of curvature of the front in the center of the specimen. The magnitude and the evolution of the curvature may differ depending on the rock fabric, but a curvature is always observed [see *David et al.*, 2011, 2008]. At the beginning of the imbibition, the water front is flat (radius of curvature greater than radius of the specimen). Then, as the water rise occurs, the front becomes more and more curved until the radius of curvature reaches a stable value (~20 mm for X2 and ~15 mm for Z1 and Z2).

3.1.2. Influence of Specimen Diameter

[16] As said previously, we used specimens with 50 mm diameter and 105 mm length. Those specimens are bigger than the ones used in previous studies [*David et al.*, 2008, 2011] which present a 40 mm diameter and 80 mm length. This difference of size gave us the opportunity to explore the effect of specimen size on the capillary imbibition process for intact specimens.

[17] The number of specimens studied with the corresponding core direction and diameter are given in Table 2. Figure 4 shows the evolution of the heights of the water front in the center (*H*) and at the border (*h*) as a function of the square root of time for all the specimens. At the beginning, *H* and *h* have a linear evolution as predicted by the linear approximation of capillary laws for small imbibed height. We observe that at any time and for each specimen the height in the center is higher than at the border. This is due to the curved shape of the water front. For the specimens characterized by a 50 mm diameter, we can see an horizontal step in the evolution of *h* around 50 mm (Figure 4b) which is due to the effect of the notch on image analysis (40 mm diameter specimens did not have notch).

[18] Except for the small anisotropy relative to coring direction [see *David et al.*, 2011], water rise kinetics in the center (Figure 4a) seems similar for all specimens without effect of specimen diameter. However, at the border there is a marked effect of specimen size (Figure 4b). Indeed, the water rise velocity at the border is always higher for small specimens (diameter of 40 mm).

3.2. Mechanical Experiments and CB Localization

3.2.1. Mechanical Data

[19] Figure 5 represents typical results obtained during a triaxial experiment on specimen Z1 (parallel to the bedding). During the loading, different stages can be separated: at the beginning the specimen has a linear response (elastic stage), then with progressive loading, the stiffness, i.e., the apparent Young's modulus, decreases and the specimen presents an inelastic response.

[20] Figure 5a represents the differential stress as a function of the axial deformation derived from the LVDT, and in the elastic stage, the Young's modulus for elastic stage can be calculated (Table 3). If we assume that the total deformation is the sum of the elastic and the inelastic deformation [*Scholz*, 1968], we can separate the elastic and the inelastic strains. Figure 5b shows the inelastic strain derived from the three strain measurements: the axial strain over the entire specimen from LVDT mounted on the piston (MTS on Figure 5), the axial deformation over a central part (60 mm) of the specimen from the extensometers (extenso on Figure 5), and the volumetric strain derived from the pore volume change (volumetric on Figure 5). As shown by *Stanchits et al.* [2009] the CB formation coincide with an increase of inelastic strain (Figure 5b). For the specimen Z1, the beginning of the CB formation probably occurs at an axial strain of ~0.65%. The three inelastic deformations measured by the three methods, which integrate deformation over different volumes, are slightly different (Figure 5). However, the differences are consistent with the fact that almost all the

Table 2. Number of Specimens Studied Depending on Core Direction and Diameter

	Parallel to Bedding (Z)	Perpendicular to Bedding (X)
40 mm diameter	3	1
50 mm diameter	2	1

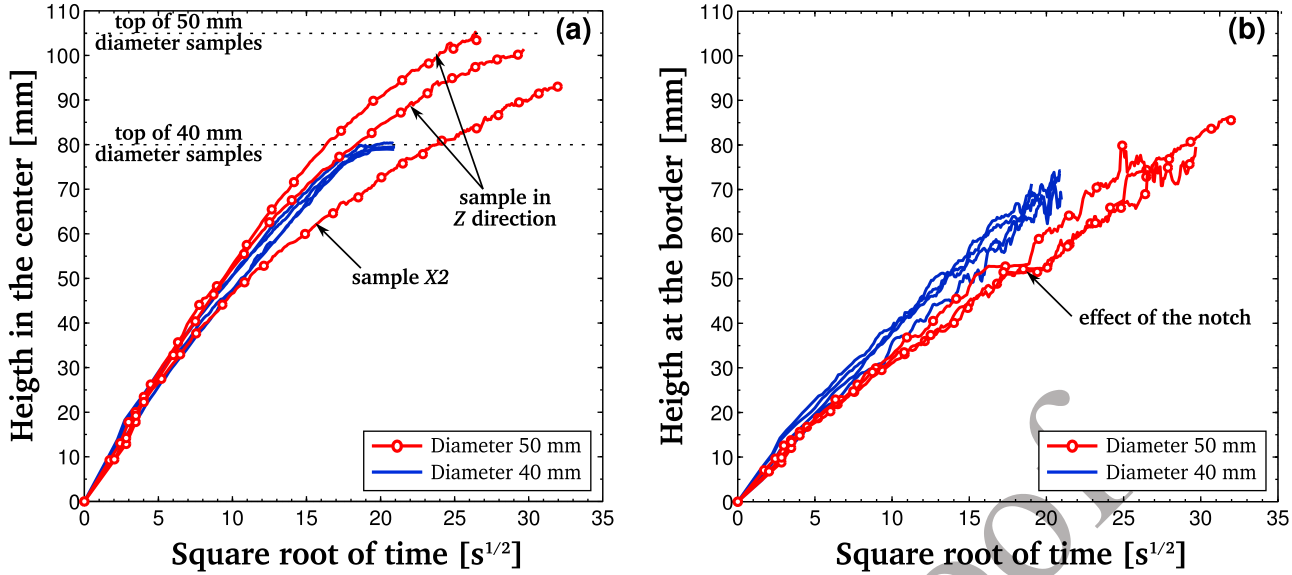

Figure 4. Evolution of heights of water for undeformed specimens as a function of square root of time. (a) Height in the center (H) and (b) height at the border (h).

inelastic deformation occurs in the CB: (1) the inelastic axial strain seen by the LVDT is lower than the inelastic strain seen by the extensometers because they measure shortening only between the upper and the lower halves of the specimen (Figure 2), whereas the LVDT measures the shortening of all the specimen; and (2) the inelastic volumetric strain measured from the pore volume variation is lower than the inelastic axial strain because of the inelastic radial strain.

[21] Then, assuming that all the inelastic deformation is concentrated in the CB, the porosity reduction in the CB, $\Delta\Phi$ can be deduced. In order to calculate this porosity reduction, we need to estimate the CB volume, in which inelastic deformation occurs. We consider it equals to the notch volume (radius r = 25 mm and thickness w_{notch} = 0.8 mm). We also assume that the volumetric strain is nearly equal to axial strain, i.e. we neglect the radial strain, an assumption which is valid in Bentheim sandstone in the light of the work of *Stanchits et al.* [2009]. Then, from the inelastic deformation, we deduce the change in volume of the CB during the test, which corresponds to the pore volume change assuming that the solid volume remains constant. The estimated porosity reduction for specimen Z1 is represented in Figure 5c using the three methods of strain measurement. The evolution of the porosity reduction is very similar whatever the measurement used and reaches at the end of the experiments a value of about 12%.

[22] The mechanical results for all the specimens (Z1, Z2 and X2) are represented in Figure 6. In Figure 6, the inelastic volumetric strain and the local porosity reduction were deduced from the pore volume change which is the most accurate method. The porosity reduction at the end of loading is about 18% for specimen X2, 12% for specimen Z1 and 6% for specimen Z2. The difference between the calculated porosity reduction for Z1 and Z2 can be explained as follows: in order to calculate the porosity reduction we use the mechanical data recorded during loading, but, for the specimen Z2 the loading was stopped before CB completion in order to have an "annular CB". However, the AE location showed that the CB formation completed during the unloading, thus we can suppose that the porosity reduction in Z2 may be similar to the estimation done in Z1. To conclude on porosity evolution, we can estimate that, after deformation, the porosity inside the specimen goes from Φ_{intact} = 22.7% in the intact parts to Φ_{CB} = 5–11% in the CB, a result similar to those obtained by *Stanchits et al.* [2009].

3.2.2. Acoustic Emissions

[23] Figure 7 shows the evolution of the AE locations during CB formation for the specimen Z1. An important point is that the geometry of CB is not planar, but composed by several layers which form a complex structure probably induced by the fact that the maximum stress due to the notch is not planar if spatial heterogeneities are present in the rock fabric [*Fortin et al.*, 2006]. During the initial stage of the loading (Figure 7a), when the response of the specimen is linear, the AE activity is quite small and the AE locations are concentrated close to the specimen top and bottom probably due to the friction between the specimen and the end pieces. In Figures 7b and 7c, AE are concentrated in the notched area, and the nucleation propagates from the border through the entire cross section (Figures 7d and 7e). In Figure 7f, the completion of the CB is marked by an increase in Young's modulus which allows us to stop the loading. Figure 8 summarizes all the AE locations for the three experiments, and we see from Figure 8a (specimen X2), Figure 8b (specimen Z1), and Figure 8c (specimen Z2) that the geometry of CB at the end of the loading looks similar for the three specimens.

3.2.3. Compaction Band Observation

[24] Figure 8 compares images from the X-ray scanner during imbibition rise and location of AE during CB formation. We can see that CB can be detected thanks to the X-ray scanner. But this observation is possible only when water has invaded the CB. Indeed, CB are not visible when the specimen is dry. Moreover, in Figure 8 we can see that there is a good agreement between X-ray observations and AE localization.

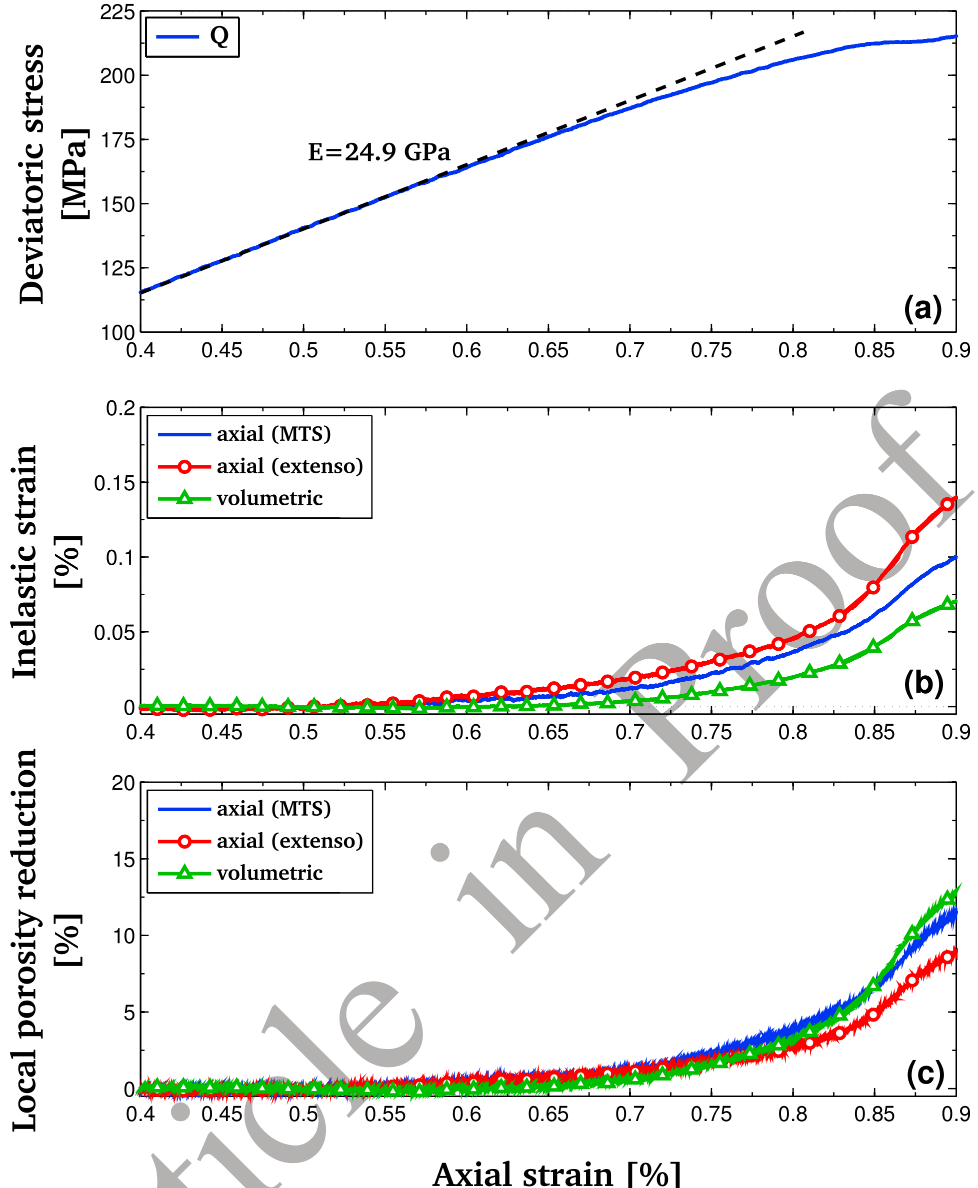

Figure 5. Mechanical data during loading for specimen Z1. (a) Loading curve and linear fit for the beginning of the load, (b) inelastic axial and volumetric strain versus axial strain, and (c) local porosity reduction versus axial strain, estimated by three strain measurements assuming that inelastic deformation is only localized in the notch area (radius r = 25 mm and thickness w_{notch} = 0.8 mm).

3.3. Capillary Imbibition Experiments on Specimens With Compaction Bands

[25] Figure 9 presents all the results of imbibition experiments for the specimens with a 50 mm diameter, with (deformed specimens) and without CB (intact specimens). Each row corresponds to a specimen and each column to a given parameter. As we focus on the impact of CB, we represent in grey the areas which are affected by CB. We estimate this volume between heights 45 mm and 60 mm from the localizations of AE (Figure 7). All this volume does not correspond to a 15 mm thick CB but because of the complex structure of the CB, this thickness must be affected by the presence of CB. Figures 9a, 9b, and 9c represent the height of water in the center (solid line) and at the border (dashed line) for intact and deformed (squares and circles) specimens. We can see that the water rise in the center is slower in specimens with CB. In addition, in deformed specimens, the water front slows down significantly in the center when it reaches the area of the CB, but the rise is also slower at the bottom of the specimen because of the damage

Table 3. Summary of Young's Modulus Measured During Elastic Stage and Local Porosity

g	X2	Z1	Z2
Young's modulus (GPa)	23.8	24.9	25
Porosity reduction at the end of loading (%)	17	12	6

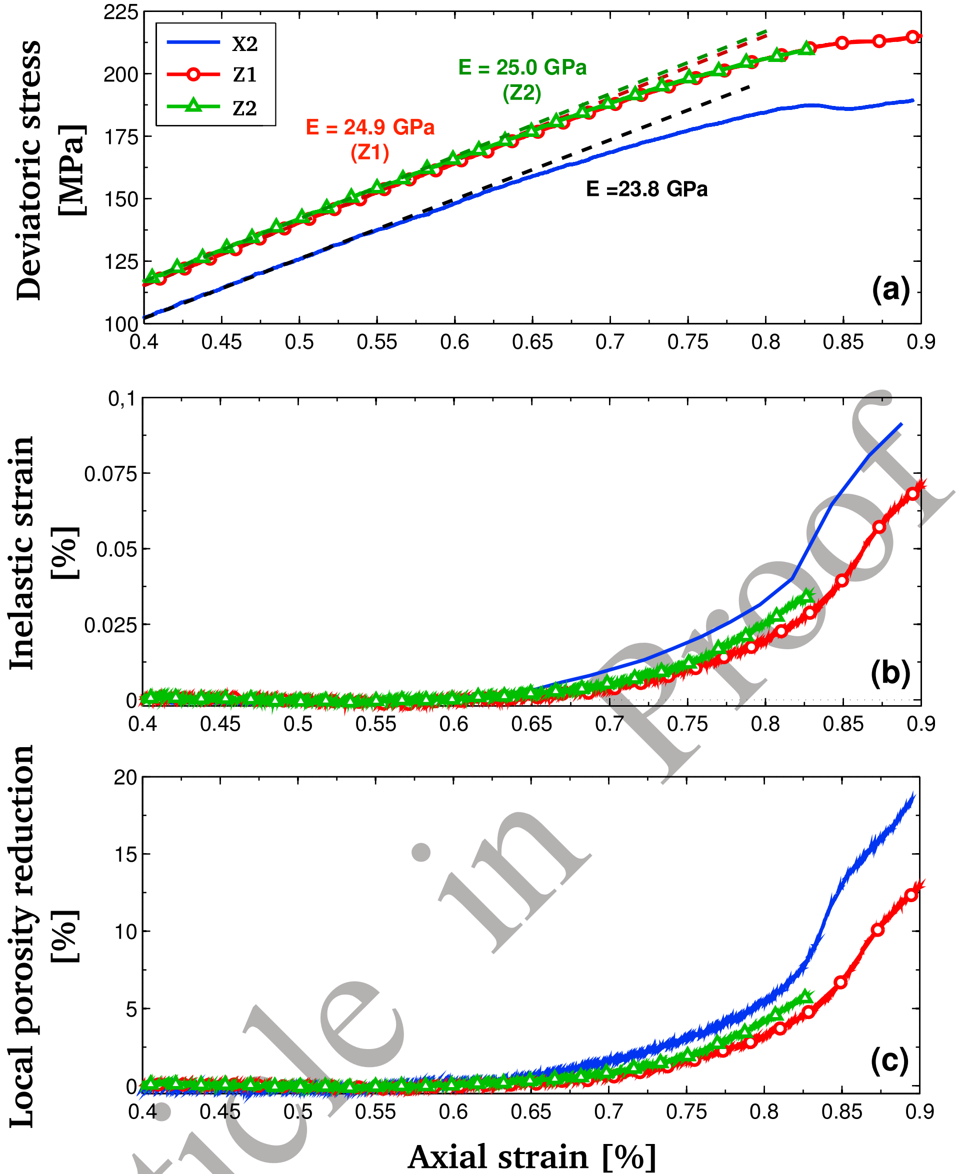

Figure 6. Mechanical data during loading for all specimens. (a) Loading curve and linear fit for the beginning of the load, (b) inelastic volumetric strain versus axial strain, and (c) local porosity reduction versus axial strain, estimated from the pore volume change, assuming that inelastic deformation is only localized in the notch area (radius r = 25 mm and thickness w_{notch} = 0.8 mm).

due to piston friction (Figure 7). The water rise at the border does not seem to be affected by the presence of CB.

[26] Consequently, a strong increase in the radius of curvature is observed when the center of the water front goes through the CB zone. This result is visible in Figures 9g, 9h, and 9i, which represent the radius of curvature of the water front in the center as a function of the square root of time. At the beginning of imbibition experiment the radius of curvature is larger for deformed specimen than for the intact ones. Then, when the water front reaches the volume affected by the CB, we observe an increase of the radius of curvature which corresponds to a flattening of the water front.

[27] Finally, Figures 9d, 9e, and 9g show the velocity of the water front in the center of the specimen as a function of the square root of time for intact and deformed (circles) specimen. To obtain this velocity, we first fit the height of water versus time using the Washburn model for capillary rise [*Washburn*, 1921]. The Washburn model expresses the time t as a function of the height H reached by the water front:

$$t(H) = \frac{H_e S \eta}{K \rho g}\left[-\ln\left(1 - \frac{H}{H_e}\right) - \frac{H}{H_e}\right], \qquad (1)$$

where $H_e = (2\gamma\,\cos(\theta))/(\rho g r_{pore})$ is the asymptotic height reached by capillary imbibition, S is the saturation of the specimen during imbibition, and K is the permeability. While $H \ll H_e = 1.4$ m (value obtained for $r_{pore} = 13.2\ \mu$m

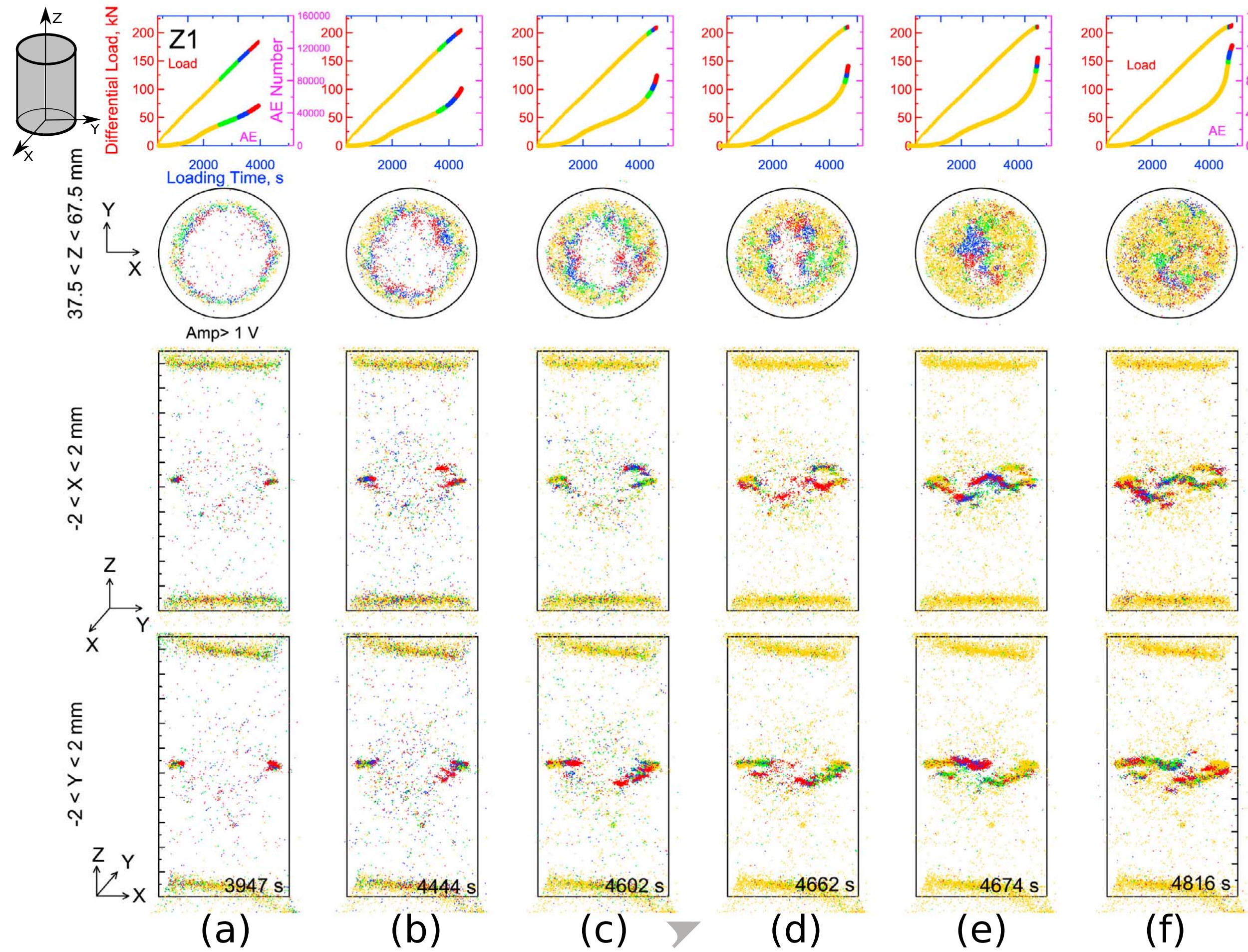

Figure 7. AE hypocenter distribution for specimen Z1. The second to fourth rows show projections of the cumulative hypocenter distribution in three different sections, divided by six time sequences (Figures 7a–f). First row shows the dependence of the differential stress and cumulative AE number versus axial strain for each time sequence. The color code is the same for all the rows, demonstrating time sequences of AE events appearance for each snapshot (Figures 7a–f). The second row shows AE events in the X-Y plane for 37.5 mm < Z < 67.5 mm). For the rest, demonstrating projections Z-Y and Z-X, we selected AE events located in a central cross section 4 mm wide.

and $\theta = 0$), using the Taylor equation, equation (1) can be inverted [*Gombia et al.*, 2008] as follows:

$$H(t) = H_e\left(1 - e^{P\left(\sqrt{t}\right)}\right), \qquad (2)$$

where P is a polynom. Here we used a second-order polynoms. Then derivation of the obtained curves give us the water front velocity. For intact specimens, such a fit presents a really good correlation coefficient, but for deformed

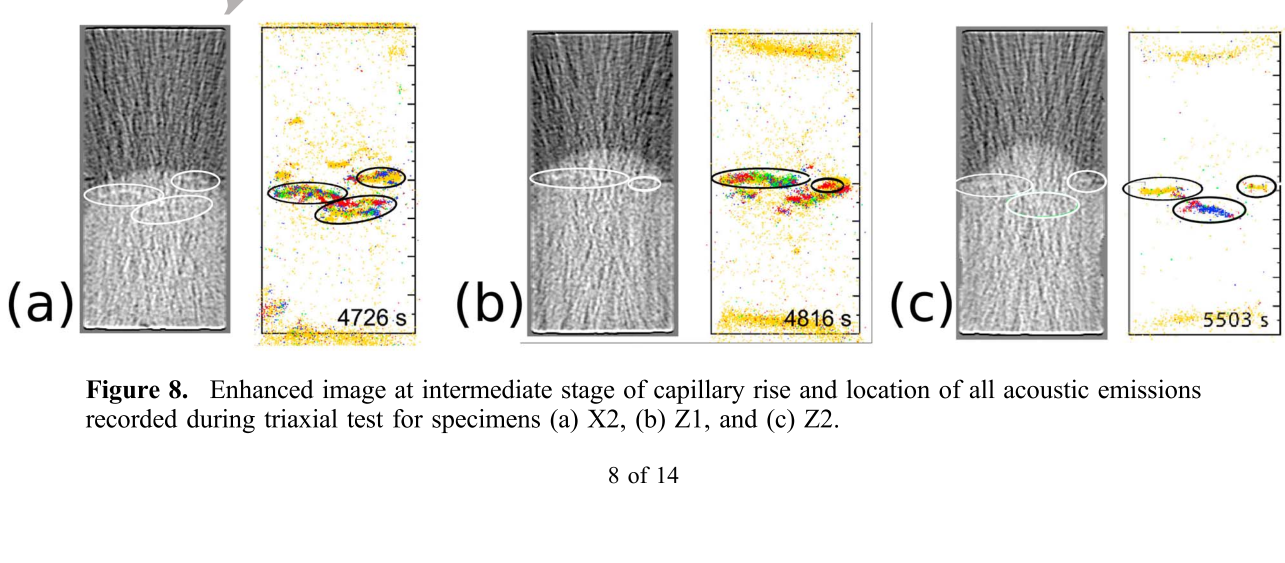

Figure 8. Enhanced image at intermediate stage of capillary rise and location of all acoustic emissions recorded during triaxial test for specimens (a) X2, (b) Z1, and (c) Z2.

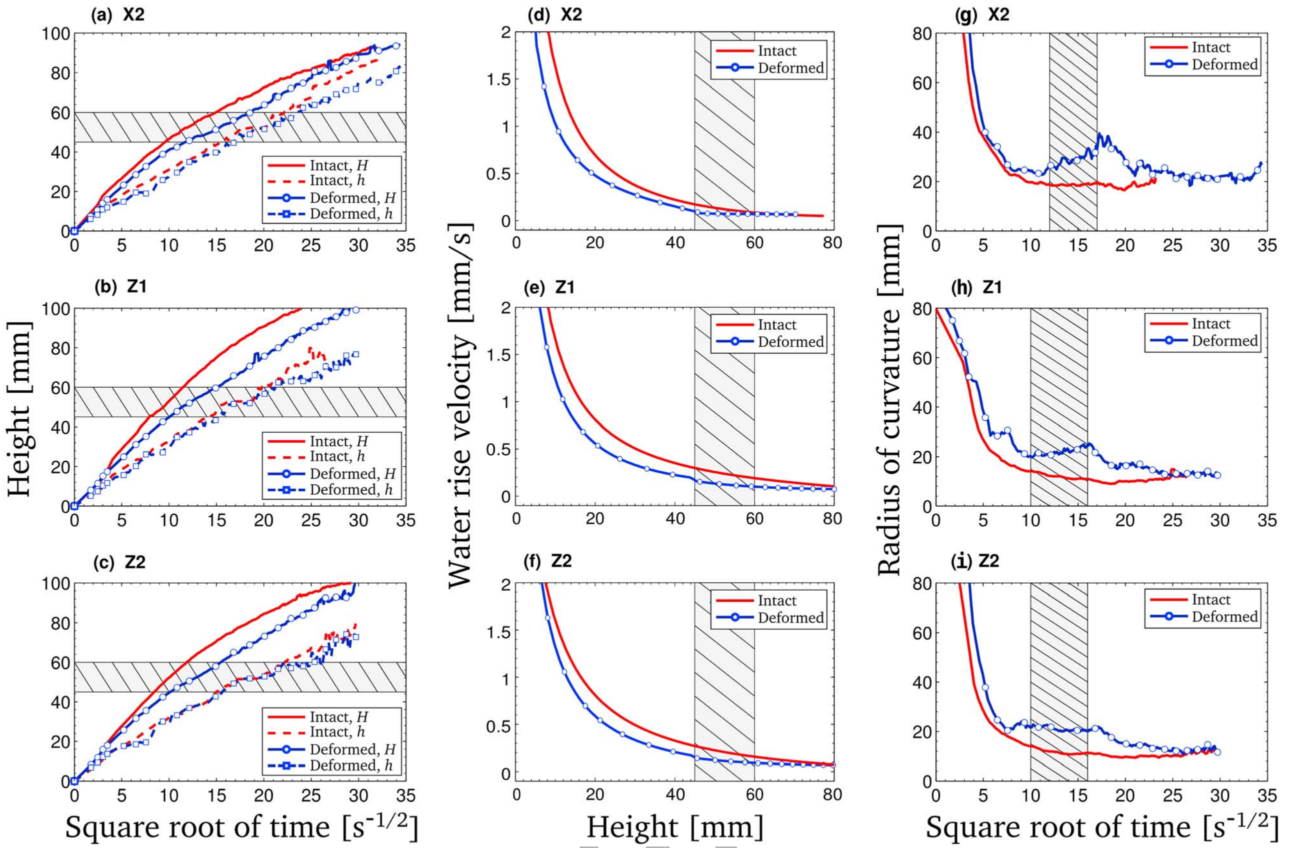

Figure 9. (a–c) Comparison of the evolution of height in the center (solid line) and at the border (dashed line) between intact (red) and deformed specimens (blue and symbols). Each row corresponds to a specimen in this order: X2, Z1, and Z2. (d–f) The water rise velocity as a function of the height in the center for intact and deformed specimens. (g–i) The evolution of the radius of curvature. The intervals corresponding to the passage of water front in the CB are represented by the gray areas (~45 mm < z < 60 mm and time intervals corresponding).

specimen, as permeability is not the same inside and outside the CB, we had to divide the time domain into two regions for the fit: the part before the water reaches the CB and the part within and beyond the CB. This technique induced a small step in velocity due to the fact that we need to adjust the two curves together. Abstracting this step, we can make two observations (Figure 9): (1) the water rise is always slower in deformed specimens than in intact specimens and (2) the velocity seems to be constant after going through the CB compared to the intact specimens in which the velocity always decreases. The asymptotic limits of the velocity are 0.050 mm/s for specimens X2 and Z2 and 0.047 mm/s for specimen Z1.

4. Discussion

[28] Our data set allows us to address a number of questions which will be discussed here. First, we will check on the effect of specimen size on the capillary imbibition results. Second, the modeling of the capillary imbibition curves will be done by including additional features linked to the curvature of the water front interface. Then we will focus on the effect of compaction bands and propose a model taking into account their specific influence on the imbibition kinetics. Doing so our model is able to fix some constraints on the permeability of compaction bands compared to that of the intact rock.

4.1. Capillary Imbibition in Intact Specimens

4.1.1. Specimen Size Effect

[29] Comparison of water front height in the center and at the surface of the specimen for two specimen sizes (Figure 4) shows an effect of specimen diameter on kinetics at the border and not in the center. Indeed, except for the small anisotropy relative to coring direction [see *David et al.*, 2011], water rise kinetics in the center is identical for all specimens. However, water rise at the border differs between specimens presenting a diameter of 40 mm or 50 mm. In Figure 4b we see that the water front at the border propagates slower for larger specimens. This observation could be linked to the boundary conditions. Indeed, at the border, there is a free boundary condition and the pressure is equal to atmospheric pressure. This results in a reduced driving force and therefore a slower imbibition kinetics. This effect should be proportional to the wet surface in contact with the atmosphere and therefore to the specimen radius. This is consistent with the observation that if we would plot the evolution of $2\pi rh$, which is the wet surface in contact with the atmosphere, as a function of $\sqrt{t}$, the graph (not shown

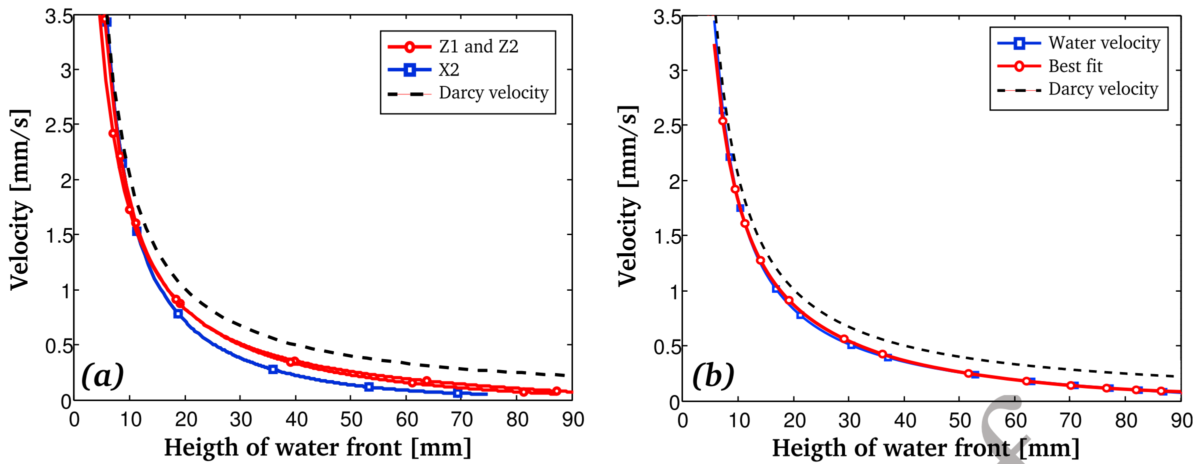

Figure 10. (a) Velocity of water front in the middle for all intact specimens as a function of the height of water in the center (solid lines) compared to Darcy velocity for r_{eq} = 13.5 μm (dashed line). (b) Velocity of water front for the specimen Z1 (squares) and the best fit using corrected Darcy law (circles).

here) would be identical independently of the specimen radius r.

[30] This specimen size dependence of the imbibition kinetics at the surface stresses the importance of measuring the kinetics inside the specimen as we do using the X-ray scanner. Studying imbibition processes from the specimen surface should therefore be done with extreme caution.

4.1.2. Kinetics of Water Imbibition

[31] Capillary imbibition is governed by two forces: capillary forces and gravity. The first one depends on the physical properties of the fluids (density and surface tension) and on the geometry of the pore network, in particular, the pore radius distribution. The second term only depends on water density.

[32] As the water velocity is not very high, flow is laminar ($Re \sim 10^{-2}$) and the flow can be described by a Darcy's flow. In first approximation, Darcy's velocity can be written

$$v(H) = \frac{K}{\eta}\left(\frac{2\gamma\cos(\theta)}{Hr_{eq}} - \rho g\right). \qquad (3)$$

Figure 10a shows the water front velocity in the center as a function of the height, H, of water front in the center for intact cases for specimens X2 (circle) and Z1 and Z2 (squares). In Darcy's law, using the hypothesis of a 3-D Poiseuille tubes assembly, the permeability K can be expressed as a function of an equivalent pore radius r_{eq} and the porosity: $K \sim (\Phi\ r_{eq}^2)/24$ [*Guéguen and Palciauskas*, 1994]. The equivalent pore radius should have the same magnitude than pore entry radius obtained by mercury porosimetry. The pore entry spectrum presents a maximum at $r = 13.5$ μm, and the values extend from ~5 μm to ~20 μm. So, we can represent Darcy velocity for the following values: Φ = 22.7% and r_{eq} = 13.5 μm (Figure 10a). For this value of r_{eq} the calculated equivalent permeability is ~1700 mdarcy which is close to the permeability measured in saturated conditions: ~1100 mdarcy (Table 1).

[33] In Figure 10a we see that a Darcy flow with the Poiseuille tubes hypothesis could fit the water imbibition as long as the water height is small ($H < 15$ mm), but for higher water height Darcy flow overestimates water rise velocity. If we compare this with the radius of curvature of the water front (Figures 9g, 9h, and 9i), we observe that Darcy velocity and real velocities diverge as soon as the water front curvature is similar to the specimen radius.

[34] Different hypothesis can explain this divergence. First, the divergence from Darcy's law can come from a variation in water saturation and so a variation in permeability during imbibition. This problem is discussed by *David et al.* [2011], and cannot be studied here with the simple Poiseuille tubes hypothesis. An other explanation can be given: due to the front curvature, not only is the flow vertical but a radial flow appears. This radial flow would slow down the water rise. Then the total flux which goes in the specimen and corresponds to the Darcy flow is divided in two fluxes: the vertical one and a radial one. And the more curved the water front is, the bigger the radial flux is. So we can assume that Darcy velocity (equation (3)) could be corrected for water front velocity in the center by

$$v(H) = \frac{K}{\eta}\left(\frac{2\gamma\cos(\theta)}{Hr_{eq}} - \rho g\right) - \frac{K_{rad}}{\eta}\rho g \alpha \frac{R}{r_c(H)}, \qquad (4)$$

where K_{rad} is the permeability in the radial direction, R is the radius of the specimen, and $r_c(H)$ is the radius of curvature of the water front which varies during imbibition and so depends on the water height, H. The second term of equation (4) corresponds to the lateral flux. R/r_c is not the exact hydraulic gradient, as r_c is a local measurement done at the center of specimen. Thus, a fitting parameter α (with no dimension) is introduced. As a consequence, we decided to simplify the equation as follows:

$$v(H) = \frac{K}{\eta}\left(\frac{2\gamma\cos(\theta)}{Hr_{eq}} - \rho g\right) - \frac{A}{r_c(H)}, \text{with } K = \frac{\Phi r_{eq}^2}{24}, \qquad (5)$$

where A is a fitting parameter expressed in m^2/s. Figure 10b represents the velocity of the water front for specimen Z1. In Figure 10b, the result from classical Darcy's law (equation (3))

Table 4. Best Fitting Parameters A, r_{eq} for All Different Situations and Height H^d the Bottom Damaged Zone

	Intact Specimens			Deformed Specimens: Damaged Part			Deformed Specimens: Compaction Band		
	X2	Z1	Z2	X2	Z1	Z2	X2	Z1	Z2
Porosity (%)	22.7	22.7	22.7	20	20	20	6	11	11
A (10^6 m^2/s)	3.4	1.1	1.4	3.4	1.1	1.4	5.2	3.0	3.0
r_{eq} (μm)	12.2	13.1	12.7	9.6	10.2	10.4	12.0	11.8	12.1
H^d (mm)	-	-	-	7	10	9	-	-	-
~K_{eq} (mdarcy)[a]	1430	1640	1550	770	870	900	480	600	670

[a]The corresponding permeability estimated by $K_{eq} = (\Phi r_{eq}^2)/24$, where K is estimated by $K = \Phi r_{eq}^2/24$.

is plotted (dashed line), and we add the best fit of the velocity with the corrected formula (equation (5)) using parameters A and r_{eq} (circles in Figure 10b) obtained by the least squares method.

[35] The best fit parameters are summarized in Table 4. We can see that for all specimens, the value of r_{eq} is really close to the value of the Hg porosimetry spectrum. We can also notice that an anisotropy exists between the two coring directions. Indeed, the parameters which characterize the permeability in the direction perpendicular to the bedding, K_X, i.e., r_{eq} for X2 and A for Z1 and Z2, are smaller than the parameters which characterize the permeability in the direction parallel to the bedding, K_Z, i.e. r_{eq} for Z1 and Z2 and A for X2. These observations are consistent with the anisotropic properties of Bentheim sandstone presented by *David et al.* [2011].

4.2. Visualization of Compaction Bands

[36] X-ray scanner is sensitive to density contrast. The gray scale of the obtained images is related to the local density at the scale corresponding to the resolution of the methods (~400 μm). Indeed, the higher the density, the lighter the image. This technique has been successfully used to visualize shear bands [e.g., *Bésuelle et al.*, 2000], where the contrast in density between the host rock and the shear localization zone is high. In the case of CB, even if there is a density contrast between the intact rock and the compaction bands zone, a direct visualization of the CB from X-ray images seems not to be possible, and previous studies used complex images analysis to observe CB structures [*Louis et al.*, 2006, 2007; *Charalampidou et al.*, 2011]. In our case, from Figure 8, we are able to see directly CB from X-ray images, and this result may be attributed to the presence of water inside the specimen. Indeed, CB can be seen when the specimen is wet but not when it is dry, which means that density contrast between intact areas and CB is higher for wet condition than for dry condition. The different densities, ρ^{dry}, and contrast density for dry condition, $\Delta\rho^{dry}$, are

$$\rho^{dry}_{intact} = (1 - \Phi_{intact})\rho_{solid}, \quad (6)$$

$$\rho^{dry}_{CB} = (1 - \Phi_{CB})\rho_{solid}, \quad (7)$$

$$\Delta\rho^{dry} = (\Phi_{intact} - \Phi_{CB})\rho_{solid}. \quad (8)$$

[37] When the specimen is invaded by the water, the contrast density, $\Delta\rho^{wet}$, is

$$\Delta\rho^{wet} = (\Phi_{intact} - \Phi_{CB})\rho_{solid} + (\Phi_{CB}S_{CB} - \Phi_{intact}S_{intact})\rho_{water}, \quad (9)$$

where S_{intact} and S_{CB} are water saturation in intact specimen and in CB, respectively. The parameter S_{intact} measured after completion of the imbibition test is about 60% due to heterogeneity in pore space dimension. This final saturation is measured by monitoring the mass of the specimen during imbibition experiment [see *David et al.*, 2011]. As CB are not observed when the specimen is dry, that means $\Delta\rho^{dry}$ is not large enough for the scanner density resolution. But we observe CB when the specimen is wet; this implies that

$$\Phi_{CB}S_{CB} - \Phi_{intact}S_{intact} > 0, \quad (10)$$

using Φ_{CB} = 15%, Φ_{intact} = 22.7% and S_{intact} = 60%, this condition is satisfied only when S_{CB} > 96%. Such a value of saturation is possible if the range of pore channel size is small. Indeed, the smaller the pores, the larger the capillary driving force for water invasion. For intact Bentheim, the pore entry spectrum presents a single peak at radius r = 13.5 μm, but the values extend from 5 to 20 μm. As a consequence, water invades preferentially the small pores, and this may explain why only 60% of the pore volume is filled with water at the end.

[38] Inside the CB, the range of pore size is reduced (the large pores are preferentially collapsed). Thus, we can assume than almost all the pore volume inside the CB is invaded and justify that S_{CB} > 96%. We try to evaluate the pore size distribution inside the CB using Hg porosimetry on a small core drilled through the region containing CB, but as the size of CB is really small and as the CB has a complex geometry, the Hg porosimetry spectrum was mostly dominated by the intact parts and almost no difference was found with the intact rock spectrum.

4.3. Effect of Damage and Compaction Band on Capillary Rise

[39] Regarding AE distribution (Figure 7), we can see that AE are concentrated in the compaction band and at the bottom and top parts of the specimen. This distribution suggests to separate specimens in different areas with different properties, as shown in Figure 11. For each zone we will consider different parameters A and r_{eq}, with linear transition between the zones. So if we know the geometry of the different zones, we need six parameters to define the specimen. In the "intact" zones where few AE were recorded, we assume that properties have not changed, so, in fact only four parameters are needed.

4.3.1. Effect of Damage Induced by End Piece Friction

[40] In order to highlight the effect of damage induced by the end piece friction, we can compare the beginning of the capillary rise before and after the mechanical test. From Figures 9d, 9e, and 9f, we see clearly in the first stage of the experiments that the water rise is slower in deformed specimens than in intact specimens. This fact suggests that the permeability, and thus pore radius, in those damaged zones is lower than in intact zones. This observation is in agree-

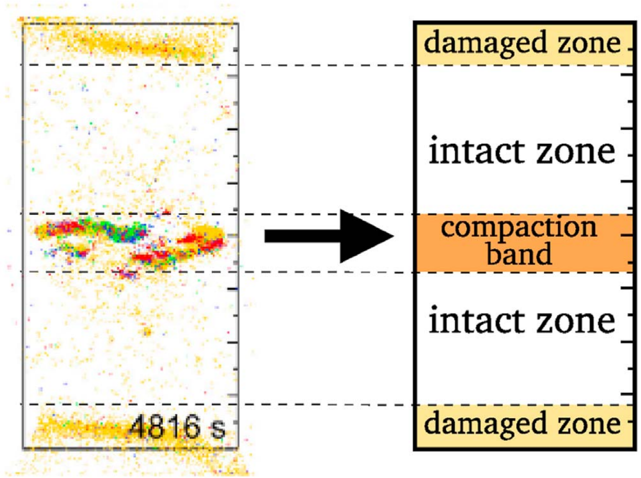

Figure 11. Distribution of the different regions for the model according to the AE localizations.

ment with the studies of *Dautriat et al.* [2009] and *Korsnes et al.* [2006], who observed such end effects.

[41] In order to quantify the permeability reduction in those zones, we focus on the velocity evolution before reaching the compaction band (H < 45 mm) for each specimen. In order to define the damaged zone, both parameters A^d and r^d_{eq}, as defined in equation (5), and H^d the height of this zones are needed. A^d is assumed to be equal to the value found in the intact zone. This assumption does not have a strong impact because the damaged zone correspond to the beginning of the imbibition (H_d < 10 mm) which presents a large radius of curvature (thus the lateral flux is almost equal to zero). Then, the only unknown parameters are H^d the height of the damage zone and r_{eq}.

[42] To compute the velocity, we assign a local permeability to the damaged zone and a local permeability to the intact zone, the global permeability $K(z)$ is calculated using a Reuss average. A reduction of permeability results in a decrease of the parameter r_{eq}.

[43] The best fitting parameters for water velocities in damaged zones are summarized in Table 4 (damaged part). Two main results are shown: (1) r_{eq} are lower in the damaged zones than in the intact parts of the rocks, which means a reduction of the permeability in the damaged zones. (2) The values found for H^d (in the range of 7–10 mm) are in agreement with the AE locations shown in Figures 7 and 11.

[44] In Figure 12b, the water front velocity and the best fit for specimen Z1 are represented. The damaged zone is defined by $H < H^d = 10$ mm.

4.3.2. Effect of Compaction Band

[45] As water dynamics inside the CB is complex and as our evaluation of the water velocity in this zone is not really accurate, we won't try to fit with accuracy the velocity in the CB but we will focus on the water velocity above the CB (i.e., H > 55 mm). Thanks to the velocity fit done before the water reaches the CB, the permeability profile is well defined in this region (H < 45 mm) and above the

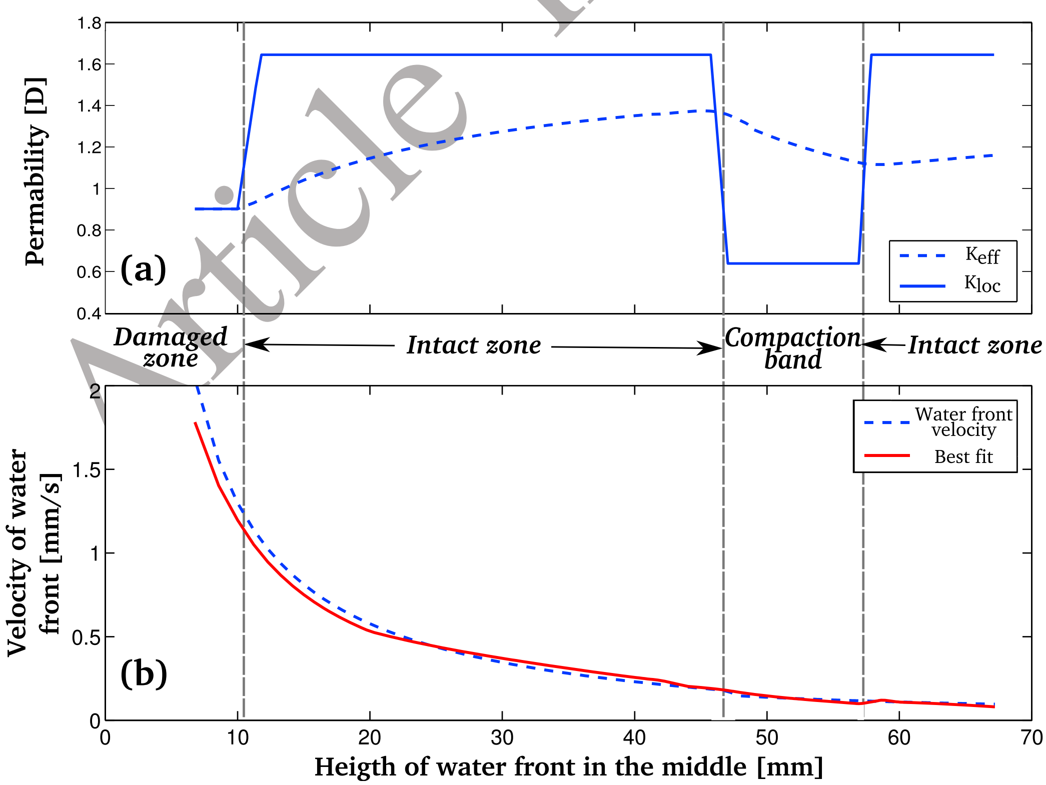

Figure 12. Results of water velocity fit for deformed specimen Z1. (a) Distribution of local permeability K_{loc} inside the specimen for the best fit (solid line) and effective permeability K_{eff} (dashed line) for the flow. (b) Comparison of velocity data (dashed line) and velocity obtained thanks to our model (solid line).

CB ($H > 55$ mm). In order to obtain the best fit of the water velocity above CB, we need the equivalent pore radius r_{eq} and the coefficient A inside the CB. The local permeability inside the CB is also calculated taking into account the porosity reduction inside the CB (Table 4).

[46] Figure 12a shows the best permeability profile which permits to fit the velocity data for specimen Z1, and Figure 12b shows the best fit of the water front velocity for the same specimen. The fit of water front velocity above the CB is constrained by the values of r_{eq} inside the CB. Indeed, as permeability inside the CB is much smaller than in the other parts, the global permeability $K(z)$ (Figure 12a) and consequently the velocity above CB are constrained by the local permeability, and thus r_{eq}, inside the CB. On the contrary the water velocity inside the CB is really dependent on the parameter A. Thus, this very simple model permits a good fit of the data, but the interpretation of all the different parameters must be done carefully.

[47] The values of r_{eq} inside the CB (Table 4) are in the same range as the values found in the intact part and do not correspond to what we should be expected from microstructural observations [*Stanchits et al.*, 2009]. This apparent inconsistency can be explained as follows: in our model we consider a CB of 10 mm thick because of the complex structure of the CB (Figure 7). Consequently the CB zone is not only composed by an effective CB, but also by some regions less damaged, and thus, our model overestimates r_{eq} inside the effective CB.

[48] Comparing permeability inside the CB, K_{CB}, and in the intact parts, K_{intact}, we can obtain an estimation of permeability reduction in the CB. This permeability is divided by 3 which is smaller than the ratio of 20–400 found by *Vajdova et al.* [2004] for Bentheim sandstone. But as said before, the estimation of permeability inside CB may be overestimated and the estimation of *Vajdova et al.* [2004] was during loading of the specimen. Moreover, field observations [*Aydin and Ahmadov*, 2009] on similar sandstone (same porosity, same order of permeability) show a permeability contrast of 5 between the CB and the host rock.

5. Conclusion

[49] To investigate the influence of compaction bands on fluid flow, we (1) conducted capillary imbibition experiments in intact Bentheim sandstone specimens (initial porosity ~ 23%), (2) then induced compaction bands (CB) in the sandstone under triaxial compression experiments done at 185 MPa effective confining pressure, and (3) conducted capillary imbibition experiments in the deformed specimens.

[50] From the mechanical data, we estimate a porosity reduction in the CB in the range of 12–18% in agreement with previous studies done on Bentheim sandstone [*Tembe et al.*, 2006; *Stanchits et al.*, 2009]. Moreover the imbibition experiments provide useful insights for a more comprehensive understanding of the coupling of compaction localization and fluid flow. Indeed, the study of capillary imbibition shows that the compaction bands clearly slow down the imbibition kinetics and disturb the geometry of water flow. These results confirm that a CB acts like a barrier for the fluid flow.

[51] Previous studies [*Louis et al.*, 2006, 2007] used complex analysis of X-ray images to observe CB structures. In our imbibition experiments, we show that a direct visualization of the CB structure from X-ray images may be possible when the specimens are wet. This observation is explained by a water saturation inside the CB close to 100%, which is possible as the porosity reduction in the localization reduces drastically the pore channel size and enhances the capillary driving forces. In addition, we show that there is a very good agreement between the AE location recorded during the triaxial experiments and the CB structure seen by the X-ray images.

[52] The direct measurement of the effect of compaction bands on the rock permeability is not obvious. In their study, *Vajdova et al.* [2004] fit the experimental data with a 1-D layered medium, with discrete layers of uniform thickness with relatively low permeability embedded in a matrix with high permeability. Using such a model, they are able to estimate the contrast of permeability between the host rock and the CB in the range of 20–400. In such model, they make the assumption that the CB is crosscutting the entire specimen.

[53] Here, to investigate the effect of compaction bands on capillary imbibition, we used notched specimens in order to induce only one localization. Using a simple model, we are able to estimate a contrast of permeability of ~3. Such a difference with the study of *Vajdova et al.* [2004] may be explained by the fact that in our case the CB does not crosscutting the entire specimen, as it may be seen from the X-ray images or the AE localization. However, it is interesting to note that the contrast of permeability found in this study is consistent with the values reported in the field [*Aydin and Ahmadov*, 2009] on similar sandstones.

[54] The existence of compaction bands has important implication on the field scale and the results of our study combining X-ray imaging during imbibition experiments and AE localization may constrain field interpretations or reservoir modeling. Indeed, the systematic organization of compaction bands within poorly consolidated sand and sandstone may result in a complex permeability structure that effectively localizes and compartmentalizes flow and subsurface fluids.

[55] **Acknowledgments.** We thank Georg Dresen for his support in this project and Stefan Gehrman (both at GFZ) for preparing the notched specimens. We also thank Jean-Christian Colombier (UCP) and Marie-Claude Lynch (IFPEN) for technical support. Finally, we thank both reviewers for their comments which helped to improve the manuscript.

References

Abramoff, M. D., P. Maglhaes, and S. Ram (2004), Image processing with ImageJ, *Biophotonics Int.*, *11*(7), 36–42.
Antonellini, M., and A. Aydin (1994), Effect of faulting on fluid flow in porous sandstones: petrophysical properties, *AAPG Bull.*, *78*, 355–377.
Aydin, A., and R. Ahmadov (2009), Bed-parallel compaction bands in aeolian sandstone: Their identification, characterization and implications, *Tectonophysics*, *479*(3–4), 277–284, doi:10.1016/j.tecto.2009.08.033.
Baud, P., E. Klein, and T.-F. Wong (2004), Compaction localization in porous sandstones: Spatial evolution of damage and acoustic emission activity, *J. Struct. Geol.*, *26*, 603–624, doi:10.1016/j.jsg.2003.09.002.
Bésuelle, P., J. Desrues, and S. Raynaud (2000), Experimental characterisation of the localisation phenomenon inside a Vosges sandstone in a triaxial cell, *Int. J. Rock Mech. Min.*, *37*(8), 1223–1237, doi:10.1016/S1365-1609(00)00057-5.
Charalampidou, E. M., S. A. Hall, S. Stanchits, H. Lewis, and G. Viggiani (2011), Characterization of shear and compaction bands in a porous sand-

stone deformed under triaxial compression, *Tectonophysics*, doi:10.1016/j.tecto.2010.09.032, in press.

Dautriat, J., N. Gland, J. Guelard, A. Dimanov, and J. L. Raphanel (2009), Axial and radial permeability evolutions of compressed sandstones: End effects and shear-band induced permeability anisotropy, *Pure Appl. Geophys.*, *166*(5–7), 1037–1061, doi:10.1007/s00024-009-0495-0.

David, C., B. Menéndez, and J.-M. Mengus (2008), Influence of mechanical damage on fluid flow patterns investigated using CT scanning imaging and acoustic emissions techniques, *Geophys. Res. Lett.*, *35*, L16313, doi:10.1029/2008GL034879.

David, C., B. Menéndez, L. Louis, and J.-M. Mengus (2011), X-ray imaging of water motion during capillary imbibition: Geometry and kinetics of water front in intact and damaged porous rocks, *J. Geophys. Res.*, doi:10.1029/2010JB007972, in press.

Fortin, J., A. Schubnel, and Y. Guéguen (2005), Elastic wave velocities and permeability evolution during compaction of Bleurswiller sandstone, *Int. J. Rock Mech. Min.*, *42*, 873–889, doi:10.1016/j.ijrmms.2005.05.002.

Fortin, J., S. Stanchits, G. Dresen, and Y. Guéguen (2006), Acoustic emission and velocities associated with the formation of compaction bands in sandstone, *J. Geophys. Res.*, *111*, B10203, doi:10.1029/2005JB003854.

Fortin, J., S. Stanchits, G. Dresen, and Y. Guéguen (2009), Acoustic emissions monitoring during inelastic deformation of porous sandstone: Comparison of three modes of deformation, *Pure Appl. Geophys.*, *166*, 823–841, doi:10.1007/s00024-009-0479-0.

Gombia, M., V. Bortolotti, R. J. S. Brown, M. Camaiti, and P. Fantazzini (2008), Models of water imbibition in untreated and treated porous media validated by quantitative magnetic resonance imaging, *J. Appl. Phys.*, *103*(9), 094913, doi:10.1063/1.2913503.

Guéguen, Y., and V. Palciauskas (1994), *Introduction to the Physics of Rocks*, Princeton Univ. Press, Princeton, N. J.

Klein, E., and T. Reuschlé (2003), A model for the mechanical behaviour of Bentheim sandstone in the brittle regime, *Pure Appl. Geophys.*, *160*(5), 833–849, doi:10.1007/PL00012568.

Klein, E., P. Baud, T. Reuschlé, and T.-F. Wong (2001), Mechanical behavior and failure mode of Bentheim sandstone under triaxial compression, *Phys. Chem. Earth, Part A*, *26*, 21–25, doi:10.1016/S1464-1895(01)00017-5.

Korsnes, R., R. Risnes, I. Faldaas, and T. Norland (2006), End effects on stress dependent permeability measurements, *Tectonophysics*, *426*, 239–251, doi:10.1016/j.tecto.2006.02.020.

Louis, L., T. Wong, P. Baud, and S. Tembe (2006), Imaging strain localization by X-ray computed tomography: Discrete compaction bands in Diemelstadt sandstone, *J. Struct. Geol.*, *28*(5), 762–775, doi:10.1016/j.jsg.2006.02.006.

Louis, L., T. Wong, and P. Baud (2007), Imaging strain localization by X-ray radiography and digital image correlation: Deformation bands in Rothbach sandstone, *J. Struct. Geol.*, *29*(1), 129–140, doi:10.1016/j.jsg.2006.07.015.

Mollema, P. (1996), Compaction bands: A structural analog for anti-mode I cracks in aeolian sandstone, *Tectonophysics*, *267*(1–4), 209–228, doi:10.1016/S0040-1951(96)00098-4.

Olsson, W. A., and D. J. Holcomb (2000), Compaction localization inporous rock, *Geophys. Res. Lett.*, *27*, 3537–3540, doi:10.1029/2000GL011723.

Scholz, C. H. (1968), Microfracturing and the inelastic deformation of rock in compression, *J. Geophys. Res.*, *73*(4), 1417–1432, doi:10.1029/JB073i004p01417.

Schultz, R. A. (2009), Scaling and paleodepth of compaction bands, Nevada and Utah, *J. Geophys. Res.*, *114*, B03407, doi:10.1029/2008JB005876.

Stanchits, S., J. Fortin, Y. Gueguen, and G. Dresen (2009), Initiation and propagation of compaction bands in dry and wet Bentheim sandstone, *Pure Appl. Geophys.*, *166*(5–7), 843–868, doi:10.1007/s00024-009-0478-1.

Sternlof, K. R., M. Karimi-Fard, D. D. Pollard, and L. J. Durlofsky (2006), Flow and transport effects of compaction bands in sandstone at scales relevant to aquifer and reservoir management, *Water Resour. Res.*, *42*, W07425, doi:10.1029/2005WR004664.

Tembe, S., V. Vajdova, T. Wong, and W. Zhu (2006), Initiation and propagation of strain localization in circumferentially notched samples of two porous sandstones, *J. Geophys. Res.*, *111*, B02409, doi:10.1029/2005JB003611.

Vajdova, V., P. Baud, and T. Wong (2004), Permeability evolution during localized deformation in Bentheim sandstone, *J. Geophys. Res.*, *109*, B10406, doi:10.1029/2003JB002942.

Van Bareen, J. P., M. W. Vos, and H. J. K. Heller (1990), Selection of outcrop specimens, internal report, Delft Univ. of Technol, Delft, Netherlands.

Washburn, E. W. (1921), The dynamics of capillary flow, *Phys. Rev.*, *17*(3), 273–283, doi:10.1103/PhysRev.17.273.

Wong, T.-f., C. David, and W. Zhu (1997), The transition from brittle faulting to cataclastic flow in porous sandstones: Mechanical deformation, *J. Geophys. Res.*, *102*, 3009–3025, doi:10.1029/96JB03281.

C. David and B. Menéndez, Laboratoire Géosciences et Environnement Cergy, Université de Cergy-Pontoise, 5 mail Gay-Lussac, F-95031 Cergy-Pontoise, France.

J. Fortin and A. Pons, Laboratoire de Géologie, École normale supérieure de Paris, UMR CNRS 8538, 24 rue Lhomond, F-75252 Paris, France. (apons@geologie.ens.fr)

J. M. Mengus, IFP Énergies Nouvelles, 1-4 av. de Bois-Préau, F-92852 Rueil-Malmaison, France.

S. Stanchits, German Research Center for Geosciences, GFZ Potsdam, Telegrafenberg D423, D-14473 Potsdam, Germany.